ORIGINAL PAPER

Fracture Initiation and Morphology of Tight Sandstone by Liquid Nitrogen Fracturing

Chunyang Hong[1] · Ruiyue Yang[1] · Zhongwei Huang[1] · Xiaozhou Qin[1] · Haitao Wen[1] · Richao Cong[1] · Wei Liu[1] · Jianxiang Chen[1]

Abstract

Hydraulic fracturing is a commonly used stimulation method in developing tight sandstone reservoirs. Creation of complex fracture networks to enlarge stimulated reservoir volume plays an increasingly significant role. However, planar fracture patterns are generally generated by water-based fluid fracturing. Besides, the water consumption and environmental burden of water-based fluid fracturing cannot be ignored. To solve the above issues, we investigated the liquid nitrogen (LN_2) fracturing performance on tight sandstone with respect to breakdown pressures and fracture network patterns, and also compared the results with water fracturing in this paper. A comprehensive quantitative analysis was made for the fracture network induced by LN_2 fracturing so as to enhance understandings of the fracturing mechanisms. Based on laboratory fracturing experiments and computed tomography (CT) scanning, we find that the breakdown pressure of LN_2 fracturing can be reduced by 12.4–51.5% compared with water fracturing. Besides, LN_2 fracturing can lead to volumetric fracturing patterns rather than planar fractures compared with water fracturing. The average tortuosity of LN_2 fracturing was increased by 5.9% compared with water fracturing. Furthermore, the major fracture tends to traverse the bedding plane with an angle of around 45–80 degrees under lower horizontal stress difference. This study, for the first time, shows potential benefits of high-pressure LN_2 fracturing in tight sandstone under triaxial in situ stress. It is expected to provide a viable alternative for the efficient development of tight sandstone reservoirs in a clean and waterless way.

Highlights

- The performance of liquid nitrogen fracturing on tight sandstone was investigated.
- A comprehensive quantitative analysis was made for the induced fractures.
- Liquid nitrogen fracturing can lower fracture initiation pressure as a comparison with water fracturing.
- Liquid nitrogen fracturing can lead to volumetric fracturing and enhance the stimulated reservoir volume.
- Major fracture tends to traverse the bedding plane with an angle under a lower horizontal stress difference.

1 Introduction

With the rapid development of horizontal well drilling and stimulation techniques, an increasing number of tight sandstone reservoirs with extremely low permeability (less than 0.1 md) were put into production (Li et al. 2021; Ma et al. 2012; Shen et al. 2017; Zou et al. 2018a). Tight oil and gas play increasingly significant roles as supplements to traditional hydrocarbon resources (Jia 2018; Liu et al. 2020, 2021a; Qiao et al. 2019). Due to the extremely low porosity and permeability, efficient stimulation technologies must be

✉ Ruiyue Yang
  yangruiyue@cup.edu.cn

✉ Zhongwei Huang
  huangzw@cup.edu.cn

1 State Key Laboratory of Petroleum Resources
  and Prospecting, China University of Petroleum, Beijing,
  China

taken to achieve effective development of tight reservoirs (Chuprakov et al. 2014; Wang et al. 2016; Wei et al. 2017). Massive hydraulic fracturing is a commonly used stimulation method, which has revolutionized the exploitation of unconventional resources around the world (Cai et al. 2020; Wang et al. 2016). The fracturing performance of tight reservoirs is affected by the bedding plane, weak planes, reservoir rock initial temperature, the in situ stress conditions and the type of fracturing fluid (Duan et al. 2020; Guo et al. 2015; Lai et al. 2017). Understanding the effects of these factors on the fracture initiation and propagation in tight sandstone is important to optimize the well completion design and thus enhance the production (Duan et al. 2020; He et al. 2017). A complex fracture network has a larger stimulated reservoir volume (SRV) which could enhance the fracture conductivity, and thus increase the oil and gas flow rate (Yang et al. 2021c). Hence, enhancing the SRV of the tight sandstone reservoirs is of critical importance for fracturing stimulation.

However, several challenges for conventional hydraulic fracturing are met, such as water consumption, reservoir damage and environmental concerns (Li et al. 2020; Middleton et al. 2015; Wang et al. 2020; Yang et al. 2021c). The reservoir is damaged mainly because water-based fracturing fluid filtrate and solute that penetrate into low-permeability reservoirs can cause clay mineral swelling, fracture and pore narrowing or blocking (Gentzis et al. 2009; Cha et al. 2018). Besides, 2-D planar fracture patterns are generally generated by the water-based fluid fracturing in tight sandstone reservoirs, which is not conducive to increasing the SRV (Duan et al. 2020; Zhang et al. 2020). Non-aqueous fracturing such as liquid/supercritical carbon dioxides (LCO$_2$/SC-CO$_2$), nitrogen gas (N$_2$) and liquid nitrogen (LN$_2$) could be a potential alternative fluid for fracturing stimulation to address these water-related issues (Yang et al. 2021a, c, 2019; Zou et al. 2018b). Among these proposed waterless fracturing methods, LN$_2$ fracturing has attracted much attention in recent years because of its special properties. The temperature of LN$_2$ is extremely low, which can reach − 196 °C under atmospheric pressure. The sudden heat transfer could cause shrinkage of the rock matrix and exert a sharp thermal gradient, which could induce numerous thermal stress cracking in tight sandstone (Cai et al. 2021). Besides, LN$_2$ poses almost no threats to the environment and can easily flow back (Huang et al. 2020b). Due to these above advantages, LN$_2$ fracturing has attracted more attention. Previous attempts have investigated the effects of LN$_2$ cooling on rock mechanical properties. Cai et al. (2014) investigated the influence of LN$_2$ cooling on pore structure in sandstone, marble, and shale specimens. The results showed that LN$_2$ cooling treatment can increase the fracturing degree inside the rocks. Zhao et al. (2017) performed laboratory investigations on the mechanical characteristics of sandstone under different conditions (dry, water, oil, mixed water and

oil saturations) before and after LN$_2$ cooling. They held the view that the damage in water-saturated sandstone was generated by the expansion of the water–ice phase transition. Du et al. (2020) explored the fracture propagation mechanism induced by LN$_2$ in sandstone with laboratory tests and numerical simulations. They confirmed that the rapid cooling induced by LN$_2$ can generate new micro-fractures and weaken the cohesion between mineral particles in sandstone. Wu et al. (2019) investigated the damage characteristics of high-temperature rocks by LN$_2$ quenching. Their findings showed that LN$_2$ can enhance the permeability of the formations and reduce the mechanical properties of rocks significantly, which is beneficial to reduce breakdown pressure and form thermally induced micro-fractures around major fractures to enhance the fracturing performance.

Besides, researchers have also focused on the fracturing performance of LN$_2$. Cha et al. (2018, 2014) developed experimental setups and procedures to conduct LN$_2$-assisted nitrogen gas fracturing (prior to fracturing with high-pressure nitrogen gas, low-pressure LN$_2$ was injected into the wellbore to induced micro-fractures) tests on shale, sandstone and concrete samples and investigated the feasibility of creating micro-fractures in the rocks surrounding a borehole. They found that the breakdown pressure levels can be significantly lowered by cryogenic treatment, and cryogenic-induced fractures around the borehole may need borehole pressurization to induce deeper fracture penetration. Wang et al. (2016) conducted LN$_2$-assisted gas fracturing on concrete samples and sandstones under no confining stress. The results indicated that the breakdown pressure of nitrogen gas fracturing after cryogenic treatment can be significantly reduced. Cai et al. (2021) examined the breakdown behaviors of sandstone induced by low-pressure LN$_2$ fracturing under the conditions of no confining pressure. They confirmed that the breakdown pressure was greatly reduced by rising the initial rock temperature. Furthermore, our previous works have conducted high-pressure LN$_2$ fracturing on synthetic coal specimens and high-temperature granite (Yang et al. 2021b, c). The results indicated that LN$_2$ fracturing can cause complex fracture networks on high-temperature granites, composed of branched fractures combined with near-wellbore thermally enhanced permeability regions. The superior performance of LN$_2$ fracturing can be attributed to the phase transition and low fluid viscosity of LN$_2$, and thermal stress induced by LN$_2$. Conclusions gathered from these previous works provided a basic understanding of LN$_2$ fracturing mechanisms.

However, sandstone belongs to sedimentary rocks, which is different from synthetic rock specimens and igneous rocks. The difference of rock mechanics and thermal properties may lead to different performances of LN$_2$ fracturing. Besides, the bedding planes have significant influences on the initiation behavior and morphology of hydraulic fractures. Chong
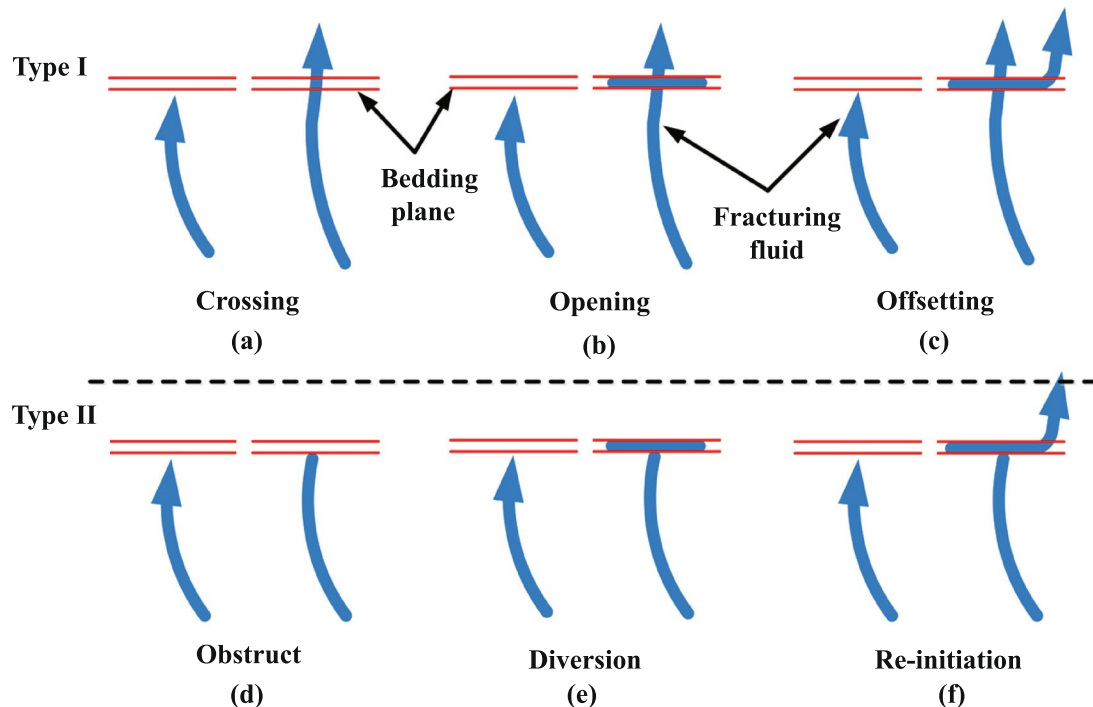
Fig. 1 The hydraulic fracture behaviors with the influence of bedding plane (Chong et al. 2017)

et al. (2017) summarized the hydraulic fracture behaviors with the influence of bedding plane, which can be divided into the following two types. In the first type (Fig. 1, type I), the fracturing fluid crosses the bedding plane directly and can be subdivided into: (a) fluid crossing the bedding plane without deflection; (b) fluid crossing the bedding plane with horizontal extension along the bedding plane; (c) fluid crossing the bedding plane with re-initiation. In the second type (Fig. 1, type II), the fracturing fluid cannot cross the bedding plane directly and can be subdivided into: (d) fluid arrested by the bedding plane; (e) fluid penetrates the bedding plane with horizontal extension; (f) fluid arrested by the bedding plane with re-initiation. Hence, it is necessary to study the performance of LN_2 fracturing on tight sandstone.

In this study, we conducted the high-pressure LN_2 fracturing tests on tight sandstone under true triaxial stresses. Fracture initiation and morphology of tight sandstone by LN_2 fracturing were investigated. Water fracturing tests were also conducted as comparisons. The full-scale non-intrusive CT scanning of rock samples after fracturing tests was also performed. A more comprehensive quantitative analysis was made for the fracture network induced by LN_2 fracturing so as to illuminate deeper understandings of the fracturing mechanism. The key findings of this work are expected to provide a theoretical guidance and laboratory experiment basis for the development of tight sandstone reservoirs in a highly efficient and environmentally accepted way.

2 Experimental Methods

2.1 Materials

All sandstone specimens used in these experiments were taken from outcrops in Yanchang Oilfield, China without visible fractures outside. First, the sandstone specimens were cut into $100 \times 100 \times 100$ mm cubes and naturally air-dried. Then, a 16-mm-diameter borehole was drilled in the middle of a specimen with a depth of 60 mm to simulate the wellbores. Two kinds of drillings were designed to explore the effects of bedding plane on the performance of LN_2 fracturing. The drilling directions parallel to the bedding plane (short as "parallel direction") and vertical to the bedding plane (short as "vertical direction") are shown in Fig. 2a and b, respectively. According to the previous works, the geological dip angle is less than 1° on Yanchang Formation of Ordos Basin (Liu et al. 2021a, b). In this paper, the vertical stress (σ_V) is perpendicular to the direction of bedding plane, in which we assume that the dip angle is 0°. Hence, the vertical stress (σ_V) was always perpendicular to the direction of the bedding plane, while the minimum horizontal
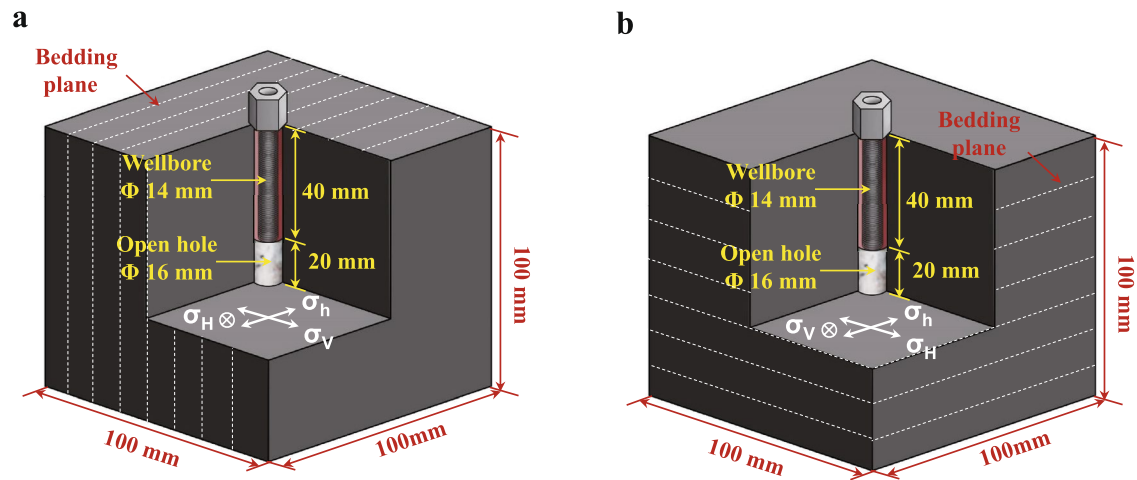
Fig. 2 Drilling direction of borehole. **a** Parallel direction; **b** vertical direction

Table 1 Basic geo-mechanical properties of the tight sandstone specimens at room temperature

Properties	Parallel direction	Vertical direction
Density (kg/m^3)	2460	2480
Uniaxial compressive strength (MPa)	99.57	110.20
Tensile strength (MPa)	9.28	4.98
Young's modulus (GPa)	22.46	19.00
Poisson's ratio	0.29	0.26
Permeability (md)	17.60×10^{-3}	13.60×10^{-3}
Porosity (%)	5.16	3.82

stress (σ_h) and maximum horizontal stress (σ_H) are always parallel to the direction of the bedding plane. Besides, the maximum horizontal stress was parallel to the drilling direction in the case of "parallel direction" to simulate fracturing in a horizontal well (Fig. 2a), while the maximum horizontal stress was perpendicular to the drilling direction in the case of "vertical direction" to simulate fracturing in a vertical well (Fig. 2b). The minimum horizontal stress was always perpendicular to the drilling direction and parallel to the direction of the bedding plane in this study. In the vertical direction, we only did one set of experiment as a comparison with the case of the horizontal direction. Finally, a 14-mm-diameter, 40-mm-length stainless steel casing was attached to the borehole with epoxy-resin adhesive. The designed open hole section was 20 mm in length and 16 mm in diameter. The specific design method of the rock samples is shown in Fig. 2.

The basic geo-mechanical properties of tight sandstone specimens in the two directions can be found in Table 1. It indicated that the tensile strength, Young's modulus,

permeability and porosity in the vertical direction were lower, but the uniaxial compressive strength was higher compared with that of parallel direction. The possible reason is that the micro-fractures in tight sandstone are mostly parallel to the bedding plane, which leads to the anisotropy of tight sandstone mechanical properties (Kim et al. 2015). Besides, the Poisson's ratio and density showed minor differences between these two directions.

2.2 Experimental System and Test Procedure

The laboratory system used in this experiment mainly consists of a true triaxial-loading system, water injection system, and high-pressure LN$_2$ injection system as shown in Fig. 3. The true triaxial-loading system can load a specimen with 100 mm in size up to 18 MPa with an accuracy of ± 0.15 MPa along the x-axis, y-axis, and z-axis. Besides, loadings on the three axes can be controlled independently. The heating tube was designed for maintaining the temperature of specimens. A reciprocating pump was used in the water injection system to inject high-pressure water into specimens with a constant rotation speed. The injection flow rate is up to 45 mm^3/min and the injection pressure is up to 45 MPa with the accuracy of ± 0.1 MPa.

The high-pressure LN$_2$ injection system was developed to inject high-pressure and low-temperature LN$_2$ into specimens. The LN$_2$ fracturing equipment mainly consists of a true triaxial-loading system, high-pressure LN$_2$ injection system, and control and data acquisition system as shown in Fig. 4. Unlike the conventional fracturing fluid which was injected by a reciprocating pump, LN$_2$ was pushed by the high-pressure nitrogen gas into boreholes to perform the fracturing test in this study due to the extremely low temperature ($-196\ ^{\circ}$C under atmospheric pressure) and properties
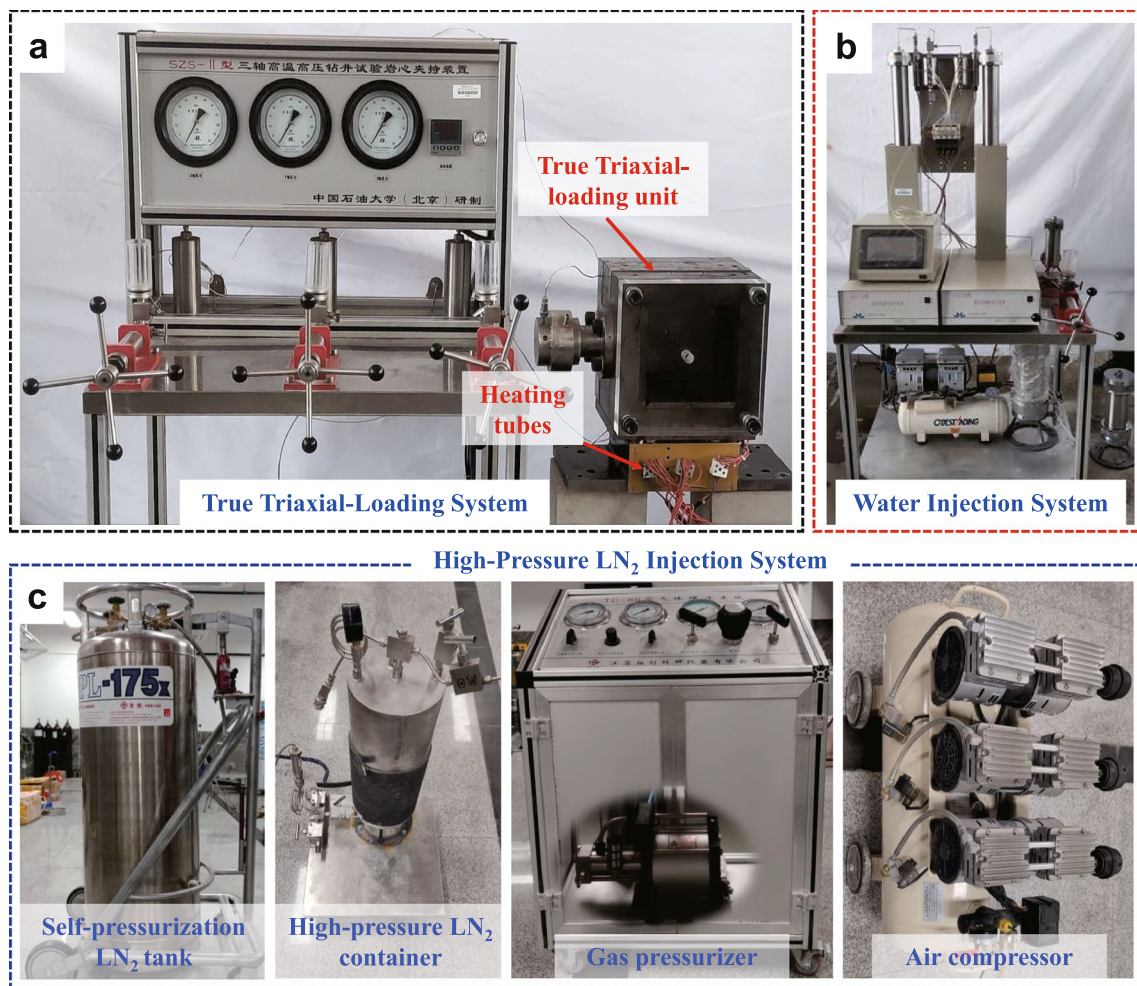
Fig. 3 True triaxial fracturing equipment. **a** True triaxial-loading system; **b** water injection system; **c** high-pressure LN₂ injection system

of easy gasification. The detailed descriptions of this newly developed laboratory system for LN₂ fracturing study under true triaxial loading and high-temperature conditions can be seen in our previous work (Yang et al. 2021b, c).

2.3 Test Procedure

In this work, two types of fracturing fluids, namely LN₂ and water, were used for comparisons under various conditions to illustrate the performance of LN₂ fracturing. In LN₂ fracturing, high-pressure and low-temperature LN₂ was injected by applying a high-pressure LN₂ injection system. The average pressurization rate (dP/dt) for LN₂ injection was about 0.40 MPa/s. In water fracturing, high-pressure water was injected by using a reciprocating pump. The injection flow rate for water fracturing was 30 mm³/min. Besides, the average pressurization rate (dP/dt) for water injection was about 0.37 MPa/s, which was close to that for LN₂ injection. The

experimental procedure for LN₂ fracturing can be found in our previous work (Yang et al. 2021b, c).

The parameters of LN₂ fracturing and water fracturing for each specimen are shown in Table 2. Totally, 14 specimens were tested under different fracturing fluids, coefficient of horizontal stress difference, sample temperature and bedding direction. The in situ stress data of tight sandstone reservoir from Yanchang Formation in the Ordos Basin, China, indicated that the horizontal stress difference is within the range of 3.0–7.0 MPa (Liu et al. 2021b). In this work, we set the horizontal stress difference as 3.0 MPa in the base case ($\sigma_H/\sigma_h/\sigma_V = 8.0/5.0/15.0$ MPa).

2.4 X-Ray Computed Tomography (CT) Scan

After fracturing tests, CT scanning system was used to observe the fracture morphology inside the fractured specimens under room temperature and atmospheric pressure conditions. Generally, the resolution decreases with the increase of specimen size (Yang et al. 2021a). Restricted by
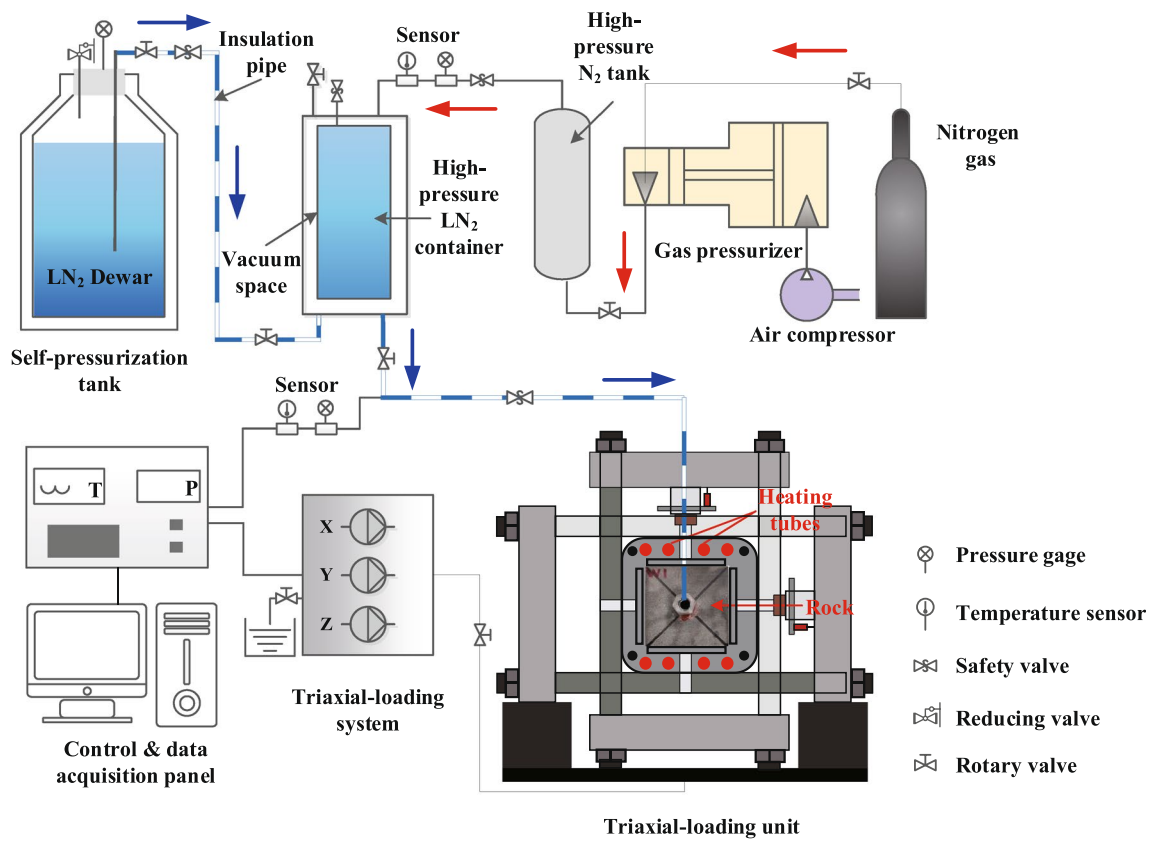
Fig. 4 Schematic of the true triaxial liquid nitrogen fracturing equipment (red arrows represent nitrogen gas transport route; blue arrows represent LN$_2$ injection into the wellbore)

Table 2 Experimental matrix for liquid nitrogen (LN$_2$) and water fracturing on tight sandstone

Sample No	Fracturing fluid	$\sigma_H/\sigma_h/\sigma_V$ (MPa)	Coefficient of horizontal stress difference*	Sample temperature (°C)	Bedding direction
LN 1	LN$_2$	8.0/5.0/15.0	0.6	100	Parallel
LN 2	LN$_2$	10.0/5.0/15.0	1.0	100	Parallel
LN 3	LN$_2$	5.3/3.3/10.0	0.6	100	Parallel
LN 4	LN$_2$	8.0/5.0/15.0	0.6	25	Parallel
LN 5	LN$_2$	8.0/5.0/15.0	0.6	200	Parallel
LN 6	LN$_2$	8.0/5.0/15.0	0.6	100	Vertical
LN 7	LN$_2$	5.0/5.0/15.0	0.0	100	Parallel
LN 8	LN$_2$	12.0/5.0/15.0	1.4	100	Parallel
W 1	water	8.0/5.0/15.0	0.6	100	Parallel
W 2	water	10.0/5.0/15.0	1.0	100	Parallel
W 3	water	5.3/3.3/10.0	0.6	100	Parallel
W 4	water	8.0/5.0/15.0	0.6	25	Parallel
W 5	water	8.0/5.0/15.0	0.6	200	Parallel
W 6	water	8.0/5.0/15.0	0.6	100	Vertical

σ_V overburden pressure, σ_H maximum horizontal stress, σ_h minimum horizontal stress
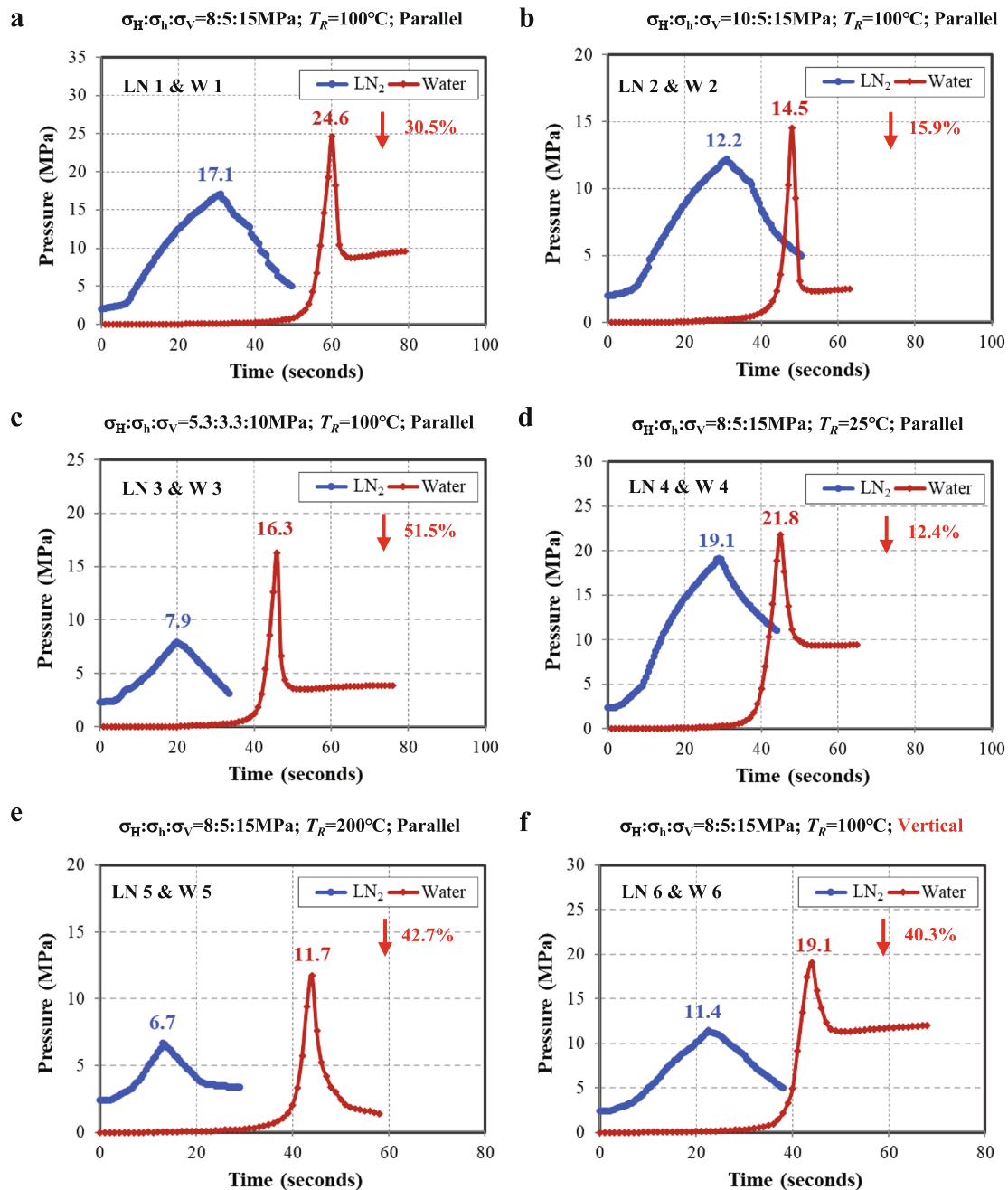
*Defined as: $(\sigma_H - \sigma_h)/\sigma_h$

Fig. 5 Pressure–time curves of the LN_2 and water fracturing tests on tight sandstone. The sample stress conditions, initial temperature (T_R) and bedding direction are: **a** $\sigma_H=8$ MPa, $\sigma_h=5$ MPa, $\sigma_V=15$ MPa, $T_R=100$ °C, parallel. **b** $\sigma_H=10$ MPa, $\sigma_h=5$ MPa, $\sigma_V=15$ MPa, $T_R=100$ °C, parallel. **c** $\sigma_H=5.3$ MPa, $\sigma_h=3.3$ MPa, $\sigma_V=15$ MPa, $T_R=100$ °C parallel. **d** $\sigma_H=8$ MPa, $\sigma_h=5$ MPa, $\sigma_V=15$ MPa, $T_R=25$ °C, parallel. **e** $\sigma_H=8$ MPa, $\sigma_h=5$ MPa, $\sigma_V=15$ MPa, $T_R=200$ °C, parallel. **f** $\sigma_H=8$ MPa, $\sigma_h=5$ MPa, $\sigma_V=15$ MPa, $T_R=100$ °C, vertical

the size of the specimens ($100 \times 100 \times 100$ mm), the voxel resolution is $40 \times 40 \times 40$ µm under an X-ray tube voltage of 270 kV and current of 350 mA. In this study, our focus is to obtain the 3D distribution of the fracture aperture to quantitatively describe the fracture morphology parameters such as aperture, surface area, volume, and deviation angle based on CT scanning.

3 Experimental Results

3.1 Breakdown Pressure

The breakdown pressure refers to the peak pressure during fluid injection, which can be used to illuminate the fracture initiation behavior under various conditions. The pressure–time curves of the LN_2 and water fracturing tests on tight sandstone are presented in Fig. 5. Before the LN_2 fracturing tests, LN_2 was injected to cool down the pipeline and wellbore at a relatively low pressure until it was discharged from the wellbore to ensure that the later injected high-pressure LN_2 is maintained at liquid state in the borehole. Besides, the LN_2 pressure in the high-pressure LN_2 container (Fig. 3c) will increase gradually, resulting from temperature increment under room temperature. Consequently, the pressure–time curves of LN_2 started at a relatively high pressure. In terms of water fracturing, after the fracturing tests, the pressure dropped rapidly and then stabilized at a relatively constant value, because water can maintain a certain pressure in the fracture with constant injection flow rate according to Darcy's law. However, after the LN_2 fracturing test, LN_2 flowed out of the fracture rapidly due to its lower viscosity and higher fracture conductivity compared with water, so that the breakdown pressure dropped rapidly. It can be found that the rock specimens were fractured with lower breakdown pressure by LN_2 as a comparison of water under the same conditions. In this experiment, LN_2 fracturing can reduce the breakdown pressure by 12.4–51.5%. The possible reason is that sharp thermal stress generated by the huge temperature difference between LN_2 and rock matrix could induce micro-fractures around the borehole and cause the pre-existing pores or micro-fractures to be connected by the newly induced fractures (Cha et al. 2018). Besides, the thermal stress generated by the cold shrinkage of rock specimen is presented in tensile stress around the wellbore

as well as the injection pressure. The tensile stress caused by the injection pressure and thermal stress is superimposed on each other, thus the fracturing fluid with lower temperature is more likely to reach the tensile failure condition (Zhang et al. 2019). Moreover, the viscosity disparity of LN_2 and water can also cause the difference in fracture initiation behavior. The lower viscosity of LN_2 has strong penetrating capacity, which make it easier to penetrate the rock matrix and propagate through micro-fractures as a comparison of water (Yang et al. 2021a). Therefore, two major complementary contributing factors, i.e., low viscosity and extremely low temperature of LN_2 reduced the breakdown pressure.

From Fig. 5a and b, we can conclude that when the coefficient of horizontal stress difference increased from 0.6 to 1, LN_2 presented 30.5% and 15.9% lower breakdown pressure than water, respectively. Besides, the breakdown pressure of LN_2 fracturing was decreased by 53.8% when the in situ stress level was decreased by 33.3%. It indicated that if rock initial temperature is given, LN_2 fracturing can reduce more breakdown pressure when rock specimens are subjected to lower horizontal stress difference or lower in situ stress level. From Fig. 5a and f, it can be found that when the drilling direction was parallel or vertical to the bedding plane, LN_2 presented 30.5% and 40.3% lower breakdown pressure than water, respectively. Furthermore, the breakdown pressures in the parallel direction was significantly larger than that of the vertical direction both in water and LN_2 fracturing when the rock initial temperature was 100 °C and the coefficient of horizontal stress difference was 0.6. Many previous studies have proved that bedding planes in tight sandstone reservoirs have significant effects on the fracture initiation and propagation performances (Ma et al. 2017; Zhang et al. 2020). In general, the numerous developed weak planes or invisible micro-fractures along the bedding plane are the main reasons for the geo-mechanical anisotropy (Huang et al. 2020a; Sato et al. 2018). Drilling along the parallel direction is more likely to connect the weak planes or invisible micro-fractures
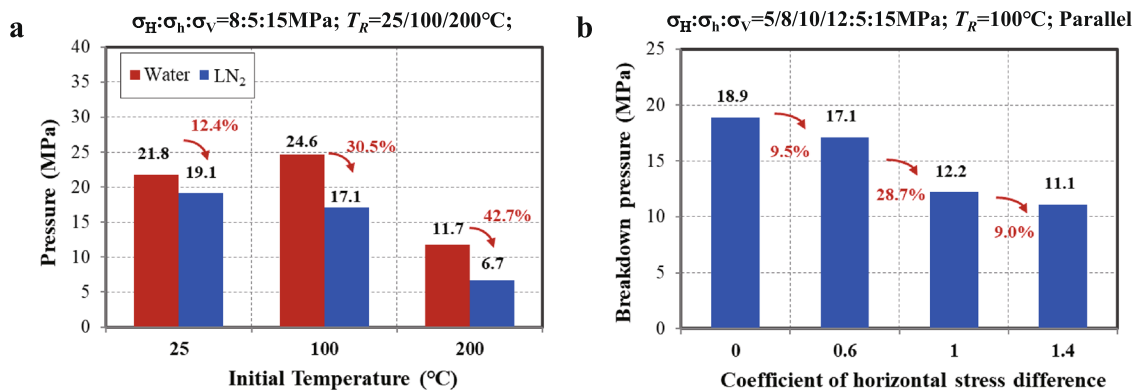

Fig. 6 Breakdown pressures of the LN_2 and water fracturing tests on tight sandstone. **a** Rock initial temperature effects on breakdown pressure; **b** stress anisotropy effects on breakdown pressure

along the bedding plane. Besides, the sharp thermal stress generated by the huge temperature difference between injection fluids and rock matrix could cause the pre-existing pores or micro-fractures to be connected by the newly induced fractures (Cha et al. 2018). However, the existence of weak planes and micro-fractures is conducive to fracture initiation and lower the breakdown pressure (Wang et al. 2017), and similar laws can be found in the fracturing tests of shale and granite according to the previous works (Wang et al. 2017, 2021; Zhou et al. 2020). Thus, the fracture initiation behavior of LN_2 fracturing has a tight relationship with the bedding plane. The effect of bedding plane on hydraulic facture initiation and propagation is suggested to be further studied before the applications in field treatment.

The rock initial temperature and stress levels have important influences on the breakdown pressure. Figure 6a shows the effects of rock initial temperature on breakdown pressure. It can be concluded that when the rock initial temperatures were 25 °C, 100 °C, and 200 °C, LN_2 presented 12.4%, 30.5% and 42.7% lower breakdown pressure than water, respectively. The reasons can be referred to in paragraph 1 of this section for details. Besides, the breakdown pressure of LN_2 fracturing showed a linear declining trend with the increase of rock initial temperature. Hence, the role of thermal stress in reducing the breakdown pressure level becomes more significant with the increase of temperature difference between rock specimens and fracturing fluid. However, when the rock initial temperature increased from 25 to 100 °C, water fracturing resulted in 12.8% higher breakdown pressure. This may be attributed to the mechanical properties of tight sandstone that was slightly promoted when the temperature increased from 25 to 260 °C (Wu et al. 2019). However, water fracturing resulted in 52.4% lower breakdown pressure when the rock initial temperature increased from 100 to 200 °C. With an increase in rock initial temperature from 100 to 200 °C, the breakdown pressure of LN_2 fracturing decreased by 60.8%. It is worthy of mention that a visible bi-wing fracture was generated in the progress of heating to 200 °C in specimens Nos. LN5 and W5, as shown in Fig. 8e (yellow solid lines). The possible reason has been analyzed in Sect. 3.2. The bi-wing fracture generated in the progress of heating was parallel to the direction of the bedding plane, which could generate high stress anisotropy or even unloading regions around the nonconformity (Wang et al. 2017). Moreover, the existence of weak planes was conducive to fracture initiation and lower the breakdown pressure (Wang et al. 2017). Hence, the breakdown pressure decreased, although the physical properties increased as the rock initial temperature increased from 100 to 200 °C.

Finally, Fig. 6b shows a linear declining trend between the coefficient of horizontal stress difference with breakdown pressure. Hence, higher coefficient of horizontal stress difference is favorable for reducing breakdown pressures in LN_2 fracturing.

3.2 Fracture Patterns and Conductivities

Generally, the final productivity of the fracture system in the field application depends on proppant distribution and placement. Many previous works focused on the proppant carrying capacity, proppant distribution and placement under various fracturing fluids by numerical simulations or experiments (Fan et al. 2020; Hou et al. 2017; Hu et al. 2018; Wen et al. 2020). Due to the limitations of the experimental conditions, we calculated the fracture conductivity of the specimens without considering proppant distribution in the fractures.

After the fracturing tests, dye solution was injected into the borehole with injection flow rate of 30 mm^3/min to color the injection-induced fractures without any confining stress. The reinjection pressure of dye solution first increased and then stabilized at a certain value. The stabilized reinjection pressure was used for the calculation of fracture conductivity (equal to the product of fracture permeability and fracture aperture). The calculation method can be expressed as (Yang et al. 2021b)

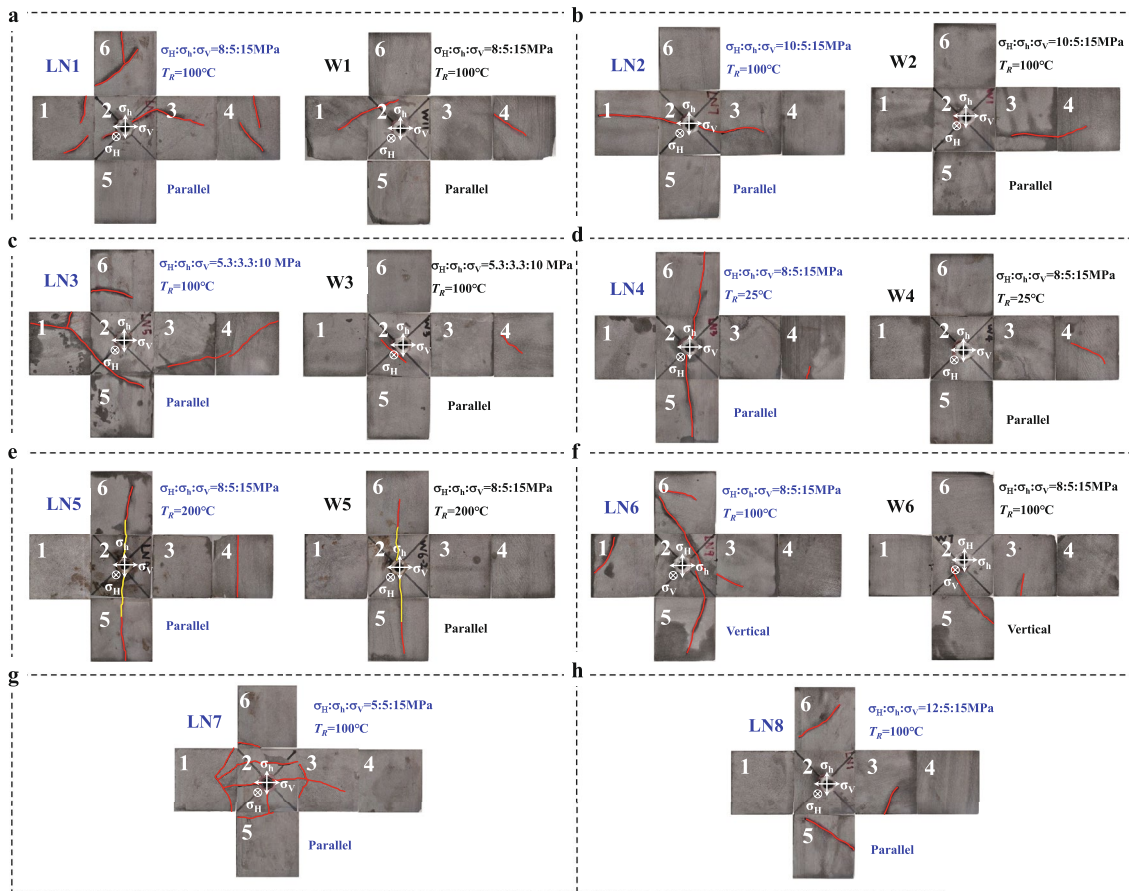**Fig. 7** Unfolded 3D graphics and fold-out diagram of a specimen
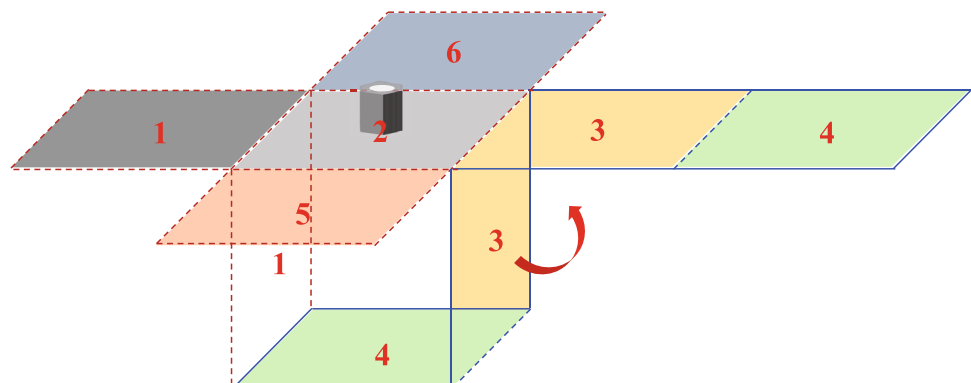
Fig. 8 Fracture patterns of tight sandstones under various fracturing conditions. **a** Specimen Nos. LN1-W1; **b** specimen Nos. LN2-W2; **c** specimen Nos. LN3-W3; **d** specimen Nos. LN4-W4; **e** specimen Nos. LN5-W5; **f** specimen Nos. LN6-W6; **g** specimen No. LN7; **h** speci-men No. LN8 (red solid lines represent the fractures; yellow solid lines represent the pre-exiting fractures before fracturing tests; white solid lines represent the direction of in situ stresses)

$$C_f = \frac{25q_{\mathrm{w}}\mu \ln\left(\frac{r_{\mathrm{e}}}{r_{\mathrm{w}}}\right)}{3\pi\Delta P_{\mathrm{wf}}}, \qquad (1)$$

where C_f is the fracture conductivity, md·mm; q_w is the flow rate, mm³/min; μ is the reinjected water viscosity, mPa s; r_{e} is the effective radius, mm, which is equal to the half length of the specimen in this study; and r_{w} is the wellbore radius, mm; ΔP_{wf} is the pressure difference between the wellbore and fracture domain, MPa.

Finally, for the presentation of fracture patterns from six surfaces simultaneously, the method of making a fold-out diagram of specimens was used as shown in Fig. 7.

Fracture patterns of tight sandstones under various frac-turing conditions were compared as shown in Fig. 8. The 3D fracture morphology and quantitative analysis by CT scan can be seen in Sect. 4.2. First, from Fig. 8a–f, it can be found that the complexity and length of induced fractures by LN_2 fracturing were significantly larger than that of water fractur-ing. This is because a huge number of micro-fractures were

induced around the borehole, which contribute to the propa-gation of fractures and the generation of complex fracture networks. When the high-temperature rock is in contact with LN_2, the volume of LN_2 will expand rapidly (nitrogen has a liquid/gas expansion ratio of 1:694 at room temperature and atmospheric pressure (Yang et al. 2021c)), which could also facilitate fracture propagation and extension.

Secondly, from Fig. 8a, c and f, it can be concluded that LN_2 fracturing can form complex fracture networks in vari-ous in situ stress level and drilling direction of borehole (specimen Nos. LN1, LN3, and LN6).

Thirdly, rock initial temperature also has important influences on the fracture propagation and patterns. When the rock initial temperature was 25 °C, a bi-wing frac-ture penetrated through specimen No. LN4, while a single short fracture was induced by water in specimen No. W4. When the rock initial temperature was 100 °C, complex fracture networks were generated in specimen No. W1, while a single longer major fracture was induced by water in specimen No. W1 as a comparison with specimen No.

W4. Hence, higher rock initial temperature was conducive to the generation of fractures both in LN_2 fracturing and water fracturing. Besides, complex fracture networks were generated by LN_2 fracturing when the rock initial temperature increased from 25 to 100 °C (specimen Nos. LN1 and LN1). However, when the rock initial temperature was 200 °C, a bi-wing fracture along the bedding plane penetrated through the specimen No. LN5, while a shorter fracture along the bedding plane was induced by water in specimen No. W5. It is worth noting that a visible bi-wing fracture along the bedding plane was marked by the yellow solid lines in Fig. 8e. The bi-wing fracture along the bedding plane before fracturing tests was induced in the progress of heating to 200 °C, owing to the nonuniform expansion of the rock matrix, epoxy-resin adhesive and wellbore. The tensile strength along the vertical direction was lower than that of the parallel direction as shown in Table 1. Once the tensile stress induced by the thermal expansion reached the tensile strength along the vertical direction, fractures along the bedding plane occurred around the wellbore. After fracturing by water and LN_2, the pre-existing fractures propagated along the bedding direction (the direction of vertical stress, σ_V) and then the pre-exiting fractures and open hole section were connected by the hydraulic fracture (red solid lines in Fig. 8e). These observations suggest that LN_2 and water injection-induced fractures preferentially initiate and propagate in the weakly bonded pre-existing fractures, even if they are opening against the maximum vertical stress (σ_V) (Wang et al. 2017).

Finally, when the coefficient of horizontal stress difference was 0, a complex fracture network was generated (specimen No. LN7), which results in a higher breakdown pressure (Fig. 6b). When the coefficient of horizontal stress difference was 0.6 (relatively lower level,

$\sigma_H/\sigma_h/\sigma_V = 8.0/5.0/15.0$ MPa), the major fracture was not perpendicular to the minimum horizontal principal stress (σ_h) as theoretically predicted, but tended to traverse the bedding plane with an angle of around 45°–80°, which can be attributed to thermal stress interference and the relative magnitude of the triaxial stresses (specimens Nos.W1, LN1, W3 and LN3). When the coefficient of horizontal stress difference was 1, the major fracture was almost perpendicular to the minimum horizontal principal stress, i.e., the fracture propagates perpendicular to the bedding plane. Similar results can be found in experiments of water fracturing in tight sandstone from Duan et al. (2020). However, when the coefficient of horizontal stress difference was 1.4 (relatively higher level, $\sigma_H/\sigma_h/\sigma_V = 12.0/5.0/15.0$ MPa), the major fracture was propagated along an angle of around 45° from the direction of the bedding plane (specimen No. LN8). This is mainly because with the increase of the horizontal stress difference, the maximum horizontal principal stress increases when the minimum horizontal principal stress is constant. Thus, the difference between the vertical stress and the maximum horizontal stress decreases, which also has a great influence on the propagation direction of the hydraulic fractures. Hence, hydraulic fractures are easier to traverse the bedding plane when the coefficient of horizontal stress difference is 1 in this study.

Figure 9d compares the fracture conductivity in specimens produced by LN_2 and water fracturing, which can be calculated using Eq. (1). It can be found that the fracture conductivities of LN_2 fracturing were significantly larger than those of water. The fracture conductivity produced in LN_2 fracturing was enhanced by 314.4% as a comparison with water on average, which further demonstrated the advantages of LN_2 fracturing in tight sandstone reservoirs.

Fig. 9 Magnitudes of fracture conductivity in specimens produced by LN_2 and water fracturing
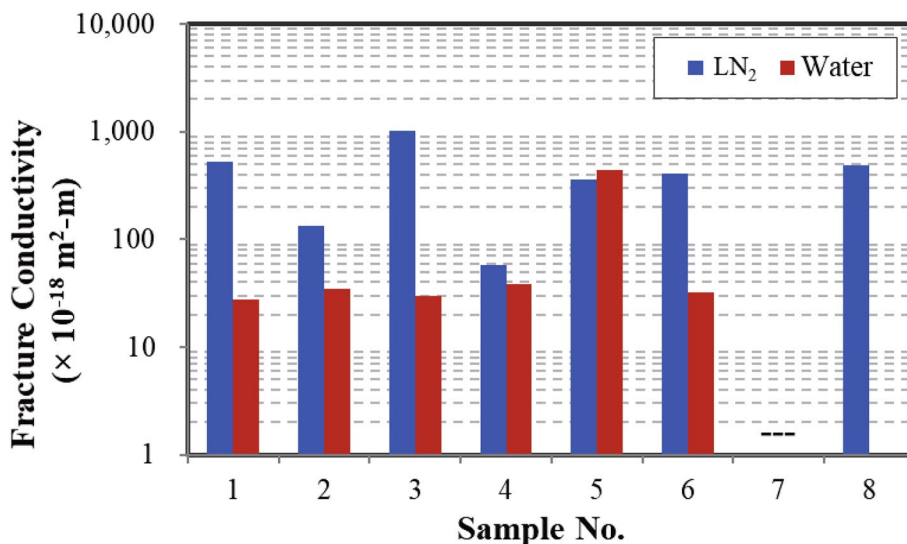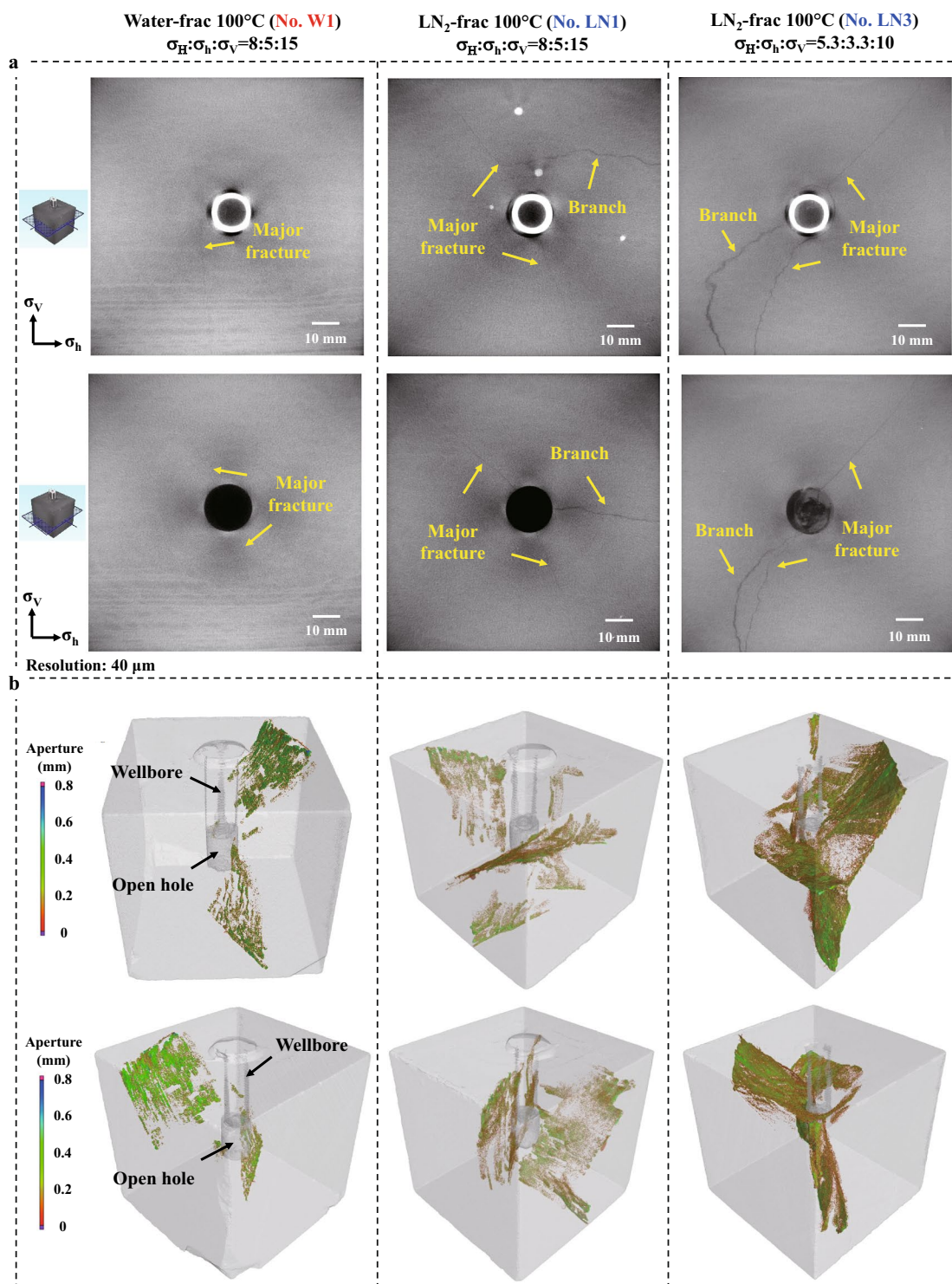
Fig. 10 CT scanning results for specimen Nos. W1, LN1 and LN3. **a** X-ray CT 2D slices in horizontal cross section; **b** 3D reconstructed fracture networks

4 Discussions

4.1 3D Reconstruction of Fracture Patterns

The CT scanning results illustrated below were used to further confirm the fracture morphology inside the rock in Sect. 3.2 and provided a reliable quantitative analysis in a non-intrusive way. The fracture patterns and profiles from different fluids and true triaxial-confining stresses were characterized in this section. After fracturing tests, three representative specimens (specimen Nos. W1, LN1 and LN3) were selected for CT scanning tests to further visualize the fracture patterns inside the rock body and quantify the fracture parameters (Fig. 10). A series of two-dimensional

slice images were obtained as shown in Fig. 10a. Then, a post-processing software was used for the 3D reconstruction of fracture patterns as shown in Fig. 10b. We can see that the fractures initiate from the open hole section of the three specimens in Fig. 10. Besides, it can be seen from Fig. 10b that the fracture morphologies on the surface of the three rock specimens were consistent with Fig. 8 basically. Some fractures initiated from the borehole and fracture branches on rock surface presented in Fig. 8 have not been shown on CT image because of the restricted resolution.

For water fractured specimen No. W1, we can see a visible bi-wing fracture perpendicular to the minimum horizontal stress direction at the specimen bottom (specimen No. W1). Then, fracture reorientation occurred at the end
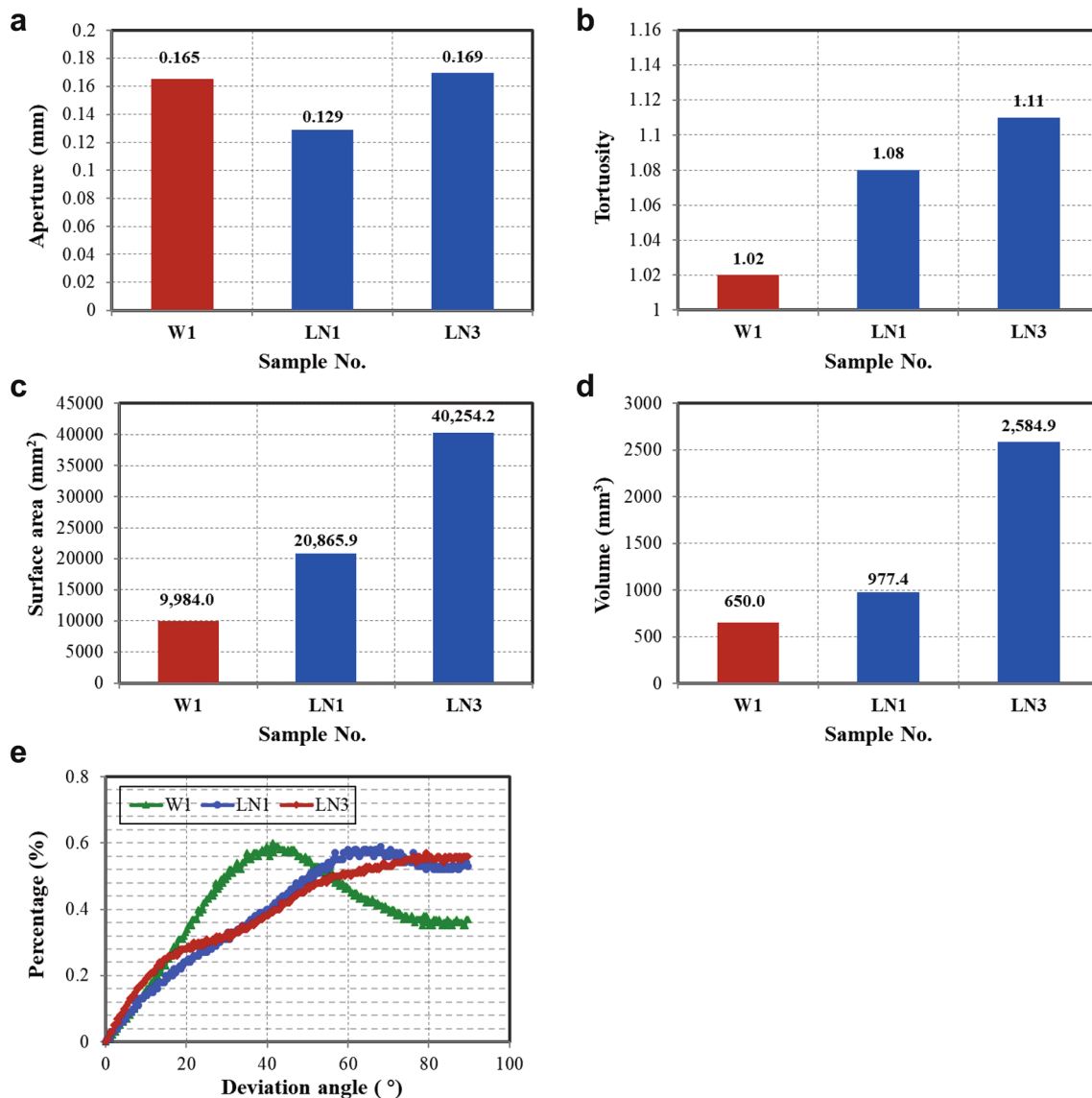

Fig. 11 Fracture parameters for specimen Nos. W1, LN1 and LN3. **a** Average aperture of the induced fractures; **b** average tortuosity of the induced fractures; **c** total surface area of the induced fractures; **d** total volumes of the induced fractures; **e** deviation angle ratio of the induced fractures

of the wellbore. For LN$_2$ fractured specimen No. LN1 and specimen No. LN3, it can be concluded that LN$_2$ fracturing produced a relatively complex fracture networks, which formed a main fracture accompanied by several fracture branches when compared with specimen No. W1. Besides, it can be concluded that the fracture connectivity of LN$_2$ fracturing was better under the condition of lower triaxial-confining stresses (the fracture conductivity of specimen No. LN3 was the largest in Fig. 9). These fractures induced by fracturing are the main pathways that can connect the isolated pores to improve the effectiveness of fluid transport space by the way (Liu et al. 2021a). Combined with the experimental results in Sect. 3.2, it can be concluded that conventional hydraulic fracturing could only cause few fractures with a relatively simple morphology, but a complex fracture network is hardly formed. LN$_2$ fracturing can lead to volumetric fracturing rather than planar fractures as a comparison with water fracturing, which is conducive to the enhancement of SRV in tight sandstone.

4.2 Quantitative Characteristic Based on Fracture Reconstruction

To evaluate the fracturing performance under various experimental conditions, the quantitative parameters of induced fractures were calculated based on 2D slices and 3D reconstruction in this section (Fig. 11).

Figure 11a compares the average aperture of the induced fractures under various conditions. The average aperture of specimen No. LN3 (0.169 mm) was the largest, followed by specimen No. W1 (0.165 mm) and specimen No. LN1 (0.129 mm). It can be found that the average aperture of LN$_2$ fracturing was smaller than that of water fracturing under the same experimental conditions (specimen Nos. W1 and LN1). The average aperture of the induced fractures by LN$_2$ fracturing was dropped by 21.8% in comparison with water fracturing. However, the fracture conductivity of specimen No. LN1 was 31 times higher than that of specimen No. W1 (Fig. 9), which indicated that more small-scale fractures were activated in LN$_2$ fracturing. Besides, wider fractures were easier to form in LN$_2$ fracturing under the condition of lower in situ stress level (specimen Nos. LN1 and LN3). The average aperture of the induced fractures was augmented by 31.0% when the in situ stress level was decreased by 33.3%.

Figure 11b compares the average tortuosity of the induced fractures under various conditions. According to the previous works, the tortuosity was defined as the ratio of the total fracture length along a pathway to the distance between the two ends of the fracture, which can be expressed as (Hou et al. 2018)

$$C = \frac{L}{L_d}, \tag{2}$$

where C is the fracture tortuosity; L is the cumulative length of the fractures, mm; L_d is the cumulative direct length between the two ends of fractures, mm.

The average tortuosity of specimen No. LN3 (1.11) was the largest, followed by specimen No. LN1 (1.08) and specimen No. W1 (1.02). It can be concluded that the average tortuosity of LN$_2$ fracturing was larger than that of water fracturing under the same experimental conditions (specimen Nos. W1 and LN1). The possible explanation is that the LN$_2$ can easily penetrate the rock matrix and micro-fractures, and open the pre-existing fractures, which may create larger fracture surface roughness (Yang et al. 2021a). In addition, the sharp thermal stress can also play an important role in the fracture reorientation. From specimen Nos. LN1 and LN3, it can be found that higher tortuosity was easier to form for LN$_2$ fracturing under the condition of lower in situ stress level. Generally, lower in situ stress level can result in more significant thermal effects. Thus, the induced fractures of LN$_2$ fracturing can cause more complex fracture networks especially under the condition of lower in situ stress level.

Figure 11c and compare the total surface area and total volumes of the induced fractures under various conditions, respectively. The total surface area and total volumes of specimen No. LN3 were the largest (40,254.2 mm^2, 2584.9 mm^3), followed by specimen No. LN1 (20,865.9 mm^2, 997.4 mm^3) and specimen No. W1 (9984.0 mm^2, 650.0 mm^3). The total surface area and total volumes of the induced fractures by LN$_2$ fracturing were increased by 109.0% and 53.4% in comparison to water fracturing, respectively (specimen Nos. W1 and LN1). The total surface area and total volumes of the induced fractures were augmented by 31.0% and when the in situ stress level was decreased by 33.3% (specimen Nos. LN1 and LN3).

The deviation angle (θ) is a parameter for the quantitative description of the 3D morphological characteristics of induced fractures, which can be expressed as

$$\theta = \cos^{-1}\left(\frac{\overrightarrow{n_f} \cdot \overrightarrow{n_p}}{\left|\overrightarrow{n_f}\right| \cdot \left|\overrightarrow{n_p}\right|} \right), \tag{3}$$

where θ is the deviation angle, °; $\overrightarrow{n_f}$ is the normal vector of medial skeleton points; $\overrightarrow{n_p}$ is the direction of the maximum horizontal principal stress.

The deflection angle is defined as the angle between the normal direction of the fracture surface and the maximum horizontal principal stress direction in this study. The vertical axis "Percentage" in Fig. 11e represents the percentage of fractures at various deviation angles. As shown in Fig. 11e, it can be found that the deflection angle of water fracturing was 40°, while that of LN$_2$ fracturing was mostly around 60°–90°. As mentioned above, the fractures tend to propagate in the direction perpendicular to the minimum principal stress, which can cause a larger deflection angle

Table 3 Comparison with previous works (Cha et al. 2018, 2017; Wang et al. 2016; Yang et al. 2021a, b, 2019)

Specimen type	Stresses (MPa)			T (°C)	Fracturing type	Fracture patterns and conductivities	Breakdown pressure	References
	σ_H	σ_h	σ_V					
Concreate/shale/ sandstone	5.2–10.4	3.5–6.9	6.9–27.6	25	LN$_2$-assisted N$_2$ gas fracturing	Micro-fractures + hydraulic fractures	LN$_2$-assisted gas fracturing was 40% lower	(Cha et al., 2018, 2017; Wang et al., 2016)
					N$_2$ gas fracturing	Hydraulic fractures		
Granite	5.0–20.0	5.0–20.0	5.0–20.0	25–600	LN$_2$ treatment + N$_2$ gas fracturing	Fracture networks	LN$_2$ treatment + gas fracturing was 9–51% lower	(Yang et al., 2019)
					N$_2$ gas fracturing	2-D planar fracture		
Synthetic-coal	4.0–12.0	2.0–7.5	5.0–15.0	25	LN$_2$ fracturing	Micro-fractures + hydraulic fractures	LN$_2$ fracturing was 10–35% lower	(Yang et al., 2021a)
					Water fracturing	2-D planar fracture		
Granite	7.6–15	3.8–11.2	22.4	25–200	LN$_2$ fracturing	Complex fracture networks, fracture conductivity produced in LN$_2$ fracturing were 5–9 times higher than N$_2$ and 10–77 times larger than water, the volumes for the induced fractures and thermally induced zones by LN$_2$ were 4 and 2.2 times higher than that fractured by water	LN$_2$ fracturing was 44% lower than water fracturing and 52% lower than N$_2$ gas fracturing	(Yang et al., 2021b)
					Water fracturing	2-D planar fracture		
					N$_2$ gas fracturing	2-D planar fracture		
Tight sandstone	5.3–12.0	3.3/5.0	10/ 15.0	25–200	LN$_2$ fracturing	Complex fracture networks, conductivity, tortuosity, surface area and volume of fractures were enhanced by 314.4%, 5.9%, 109.0% and 53.4%, respectively	LN$_2$ fracturing was 12.4–51.5% lower	(This study)
					Water fracturing	Bi-wing fracture		

T rock initial temperature

(specimen Nos. LN1 and LN3). However, the existence of natural weak planes has significance influence on the propagation of fractures. Hence, the smaller deflection angle was attributed to the irregularities of pre-existing fractures or experimental error (specimen No. W1 in Fig. 10b).

4.3 Comparison with Previous Works

The comparisons of fracture patterns, fracture conductivities and breakdown pressure related to LN$_2$ fracturing with previous works and this study are shown in Table 3. We can find that the research using LN$_2$ as fracturing fluid can

be divided into the three types: (a) LN_2-assisted nitrogen (N_2) gas fracturing (prior to fracturing with high-pressure nitrogen gas, low-pressure LN_2 was injected into the wellbore to induce micro-fractures) (Cha et al. 2017, 2018; Wang et al. 2016); (b) LN_2 treatment before N_2 gas fracturing (prior to fracturing with high-pressure nitrogen gas, single or cycle LN_2 cooling treatment was done to induce micro-fractures) (Yang et al. 2019); (c) LN_2 fracturing (using LN_2 directly as the fracturing fluid) (Yang et al. 2021b, c). Compared with water fracturing or N_2 gas fracturing, the above three methods can reduce the breakdown pressure and increase the complexity of fracture networks. Besides, the third type was the best among these three methods. In this paper, we make up for the deficiency in the study of LN_2 fracturing on tight sandstone. Besides, we make a more comprehensive quantitative analysis for the fracture network induced by LN_2 fracturing so as to illuminate deeper understandings of the fracturing mechanism. This has been achieved by investigating the aperture, tortuosity, surface area and volume of fractures by CT scanning.

5 Conclusions

In this paper, we conducted LN_2 fracturing experiments on tight sandstone. The breakdown pressures and fracture patterns were investigated under various rock initial temperature and true triaxial stresses. Finally, the fracture parameters including aperture, tortuosity, surface area, volumes and deflection angle were quantitative analyzed by CT scanning so as to illuminate deeper understandings of the fracturing mechanism. The key conclusions can be summarized as follows:

- The breakdown pressure of LN_2 fracturing can be reduced by 12.4–51.5% as a comparison with water fracturing under various in situ stress levels and rock initial temperatures. LN_2 fracturing can reduce more breakdown pressure when tight sandstone specimens are subjected to lower horizontal stress difference or in situ stress level and higher rock initial temperature.
- LN_2 fracturing can lead to volumetric fracturing rather than planar fractures as a comparison of water fracturing, which is conducive to the enhancement of SRV in tight sandstone. The conductivity, tortuosity, surface area and volume of fractures can be significantly enhanced by 314.4%, 5.9%, 109.0% and 53.4%, respectively, while the fracture aperture deceased by 21.8% because more small-scale fractures were activated. Besides, LN_2 fracturing can induce more complex fracture networks when tight sandstone specimens are

subjected to lower horizontal stress difference or lower in situ stress level and higher rock initial temperature.
- The breakdown pressure of drilling parallel to the bedding plane was significantly larger than vertical direction both in water and LN_2 fracturing when the rock initial temperature is 100 °C and the coefficient of horizontal stress difference is 0.6. The major fracture tends to traverse the bedding plane with an angle of around 45°–80° under lower horizontal stress difference, which can be attributed to thermal stress interference and the relative magnitude of the triaxial stresses. Besides, the major fracture was easier to traverse the bedding plane when the coefficient of horizontal stress difference was 1 in this study.
- The obtained results in this study were based on the laboratory-scale investigation. The fracturing performance of LN_2 in tight sandstone should be further verified by field applications.

References

Cai C, Li G, Huang Z, Shen Z, Tian S, Wei J (2014) Experimental study of the effect of liquid nitrogen cooling on rock pore structure. J Nat Gas Sci Eng 21:507–517

Cai J, Li C, Song K, Zou S, Yang Z, Shen Y, Meng Q, Liu Y (2020) The influence of salinity and mineral components on spontaneous imbibition in tight sandstone. Fuel 269.

Cai C, Tao Z, Ren K, Liu S, Yang Y, Feng Y, Su S, Hou P (2021) Experimental investigation on the breakdown behaviours of sandstone due to liquid nitrogen fracturing. J Pet Sci Eng 200

Cha M, Yin X, Kneafsey T, Johanson B, Alqahtani N, Miskimins J, Patterson T, Wu Y-S (2014) Cryogenic fracturing for reservoir stimulation—laboratory studies. J Petrol Sci Eng 124:436–450

Cha M, Alqahtani NB, Yin X, Kneafsey TJ, Yao B, Wu Y-S (2017) Laboratory system for studying cryogenic thermal rock fracturing for well stimulation. J Petrol Sci Eng 156:780–789

Cha M, Alqahtani NB, Yao B, Yin X, Kneafsey TJ, Wang L, Wu Y, Miskimins JL (2018) Cryogenic fracturing of wellbores under true triaxial-confining stresses: experimental investigation. SPE J 23(04):1271–1289

Chong Z, Karekal S, Li X, Hou P, Yang G, Liang S (2017) Numerical investigation of hydraulic fracturing in transversely isotropic shale reservoirs based on the discrete element method. J Nat Gas Sci Eng 46:398–420

Chuprakov D, Melchaeva O, Prioul R (2014) Injection-sensitive mechanics of hydraulic fracture interaction with discontinuities. Rock Mech Rock Eng 47(5):1625–1640

Du M, Gao F, Cai C, Su S, Wang Z (2020) Study on the surface crack propagation mechanism of coal and sandstone subjected to cryogenic cooling with liquid nitrogen. J Nat Gas Sci Eng 81

Duan W, Sun B, Pan D, Wang T, Guo T, Wang Z (2020) Experimental study on fracture propagation of hydraulic fracturing for tight sandstone outcrop. Energy Explor Exploit 39(1):156–179

Guo C, Xu J, Wei M, Jiang R (2015) Experimental study and numerical simulation of hydraulic fracturing tight sandstone reservoirs. Fuel 159:334–344

He J, Lin C, Li X, Zhang Y, Chen Y (2017) Initiation, propagation, closure and morphology of hydraulic fractures in sandstone cores. Fuel 208:65–70

Hou P, Gao F, Gao Y, Yang Y, Cai C (2018) Changes in breakdown pressure and fracture morphology of sandstone induced by nitrogen gas fracturing with different pore pressure distributions. Int J Rock Mech Min Sci 109:84–90

Huang D, Li B, Ma W-Z, Cen D-F, Song Y-X (2020a) Effects of bedding planes on fracture behavior of sandstone under semi-circular bending test. Theoret Appl Fract Mech 108

Huang Z, Zhang S, Yang R, Wu X, Li R, Zhang H, Hung P (2020b) A review of liquid nitrogen fracturing technology. Fuel 266

Jia A (2018) Progress and prospects of natural gas development technologies in China. Nat Gas Ind B 5(6):547–557

Kim KY, Zhuang L, Yang H, Kim H, Min K-B (2015) Strength anisotropy of berea sandstone: results of X-ray computed tomography, compression tests, and discrete modeling. Rock Mech Rock Eng 49(4):1201–1210

Lai J, Wang G, Fan Z, Wang Z, Chen J, Zhou Z, Wang S, Xiao C (2017) Fracture detection in oil-based drilling mud using a combination of borehole image and sonic logs. Mar Pet Geol 84:195–214

Li X, Huang W, Sun J, Li X, Jia J, Duan W, Sun J (2020) Wettability alteration and mitigating aqueous phase trapping damage in tight gas sandstone reservoirs using mixed cationic surfactant/nonionic fluoro-surfactant solution. J Pet Sci Eng 195

Li Q, Li Y, Gao S, Liu H, Ye L, Wu H, Zhu W, An W (2021) Well network optimization and recovery evaluation of tight sandstone gas reservoirs. J Pet Sci Eng 196

Liu J, Hui C, Fan J, Lyu W, Wang J, Yin C, Wang H (2021b) Distribution characteristics of the present-day in-situ stress in the Chang 6 tight sandstone reservoirs of the Yanchang Formation in the Heshui Area, Ordos Basin, China and suggestions for development. J Geomech 27:31–39

Liu G, Meng Z, Luo D, Wang J, Gu D, Yang D (2020) Experimental evaluation of interlayer interference during commingled production in a tight sandstone gas reservoir with multi-pressure systems. Fuel 262.

Liu G, Zeng L, Zhu R, Gong L, Ostadhassan M, Mao Z (2021a) Effective fractures and their contribution to the reservoirs in deep tight sandstones in the Kuqa Depression, Tarim Basin, China. Marine and Petroleum Geology 124.

Ma X, Jia A, Tan J, He D (2012) Tight sand gas development technology and practices in China. Pet Explor Dev 39(5):611–618

Ma X, Zhou T, Zou Y (2017) Experimental and numerical study of hydraulic fracture geometry in shale formations with complex geologic conditions. J Struct Geol 98:53–66

Middleton RS, Carey JW, Currier RP, Hyman JD, Kang Q, Karra S, Jiménez-Martínez J, Porter ML, Viswanathan HS (2015) Shale gas and non-aqueous fracturing fluids: opportunities and challenges for supercritical CO_2. Appl Energy 147:500–509

Qiao J, Zeng J, Jiang S, Feng S, Feng X, Guo Z, Teng J (2019) Heterogeneity of reservoir quality and gas accumulation in tight sandstone reservoirs revealed by pore structure characterization and physical simulation. Fuel 253:1300–1316

Sato M, Panaghi K, Takada N, Takeda M (2018) Effect of bedding planes on the permeability and diffusivity anisotropies of berea sandstone. Transp Porous Media 127(3):587–603

Shen Y, Lü X, Guo S, Song X, Zhao J (2017) Effective evaluation of gas migration in deep and ultra-deep tight sandstone reservoirs

of Keshen structural belt, Kuqa depression. J Nat Gas Sci Eng 46:119–131

Wang L, Yao B, Cha M, Alqahtani NB, Patterson TW, Kneafsey TJ, Miskimins JL, Yin X, Wu Y-S (2016) Waterless fracturing technologies for unconventional reservoirs-opportunities for liquid nitrogen. J Nat Gas Sci Eng 35:160–174

Wang L, Yao B, Xie H, Winterfeld PH, Kneafsey TJ, Yin X, Wu Y-S (2017) CO2 injection-induced fracturing in naturally fractured shale rocks. Energy 139:1094–1110

Wang J, Huang Y, Zhou F, Song Z, Liang X (2020) Study on reservoir damage during acidizing for high-temperature and ultra-deep tight sandstone. J Pet Sci Eng 191

Wang J, Xie H, Li C (2021) Anisotropic failure behaviour and breakdown pressure interpretation of hydraulic fracturing experiments on shale. Int J Rock Mech Min Sci 142

Wei D, Gao Z, Fan T, Wang S, Li C, Li H (2017) Experimental hydraulic fracture propagation on naturally tight intra-platform shoal carbonate. J Petrol Sci Eng 157:980–989

Wu X, Huang Z, Zhang S, Cheng Z, Li R, Song H, Wen H, Huang P (2019) Damage analysis of high-temperature rocks subjected to LN2 thermal shock. Rock Mech Rock Eng 52(8):2585–2603

Yang R, Huang Z, Shi Y, Yang Z, Huang P (2019) Laboratory investigation on cryogenic fracturing of hot dry rock under triaxial-confining stresses. Geothermics 79:46–60

Yang R, Hong C, Huang Z, Wen H, Li X, Huang P, Liu W, Chen J (2021b) Liquid nitrogen fracturing in boreholes under true triaxial stresses: laboratory investigation on fractures initiation and morphology. SPE J 26(01):135–154

Yang R, Hong C, Liu W, Wu X, Wang T, Huang Z (2021c) Non-contaminating cryogenic fluid access to high-temperature resources: liquid nitrogen fracturing in a lab-scale enhanced geothermal system. Renew Energy 165:125–138

Yang B, Wang H, Wang B, Shen Z, Zheng Y, Jia Z, Yan W (2021a) Digital quantification of fracture in full-scale rock using micro-CT images: a fracturing experiment with N_2 and CO_2. J Pet Sci Eng 196

Zhang W, Guo T-k, Qu Z-q, Wang Z (2019) Research of fracture initiation and propagation in HDR fracturing under thermal stress from meso-damage perspective. Energy 178:508–521

Zhang Q, Zhang X-P, Sun W (2020) Hydraulic fracturing in transversely isotropic tight sandstone reservoirs: A numerical study based on bonded-particle model approach. J Struct Geol 136

Zhao B, Zhang G-q, Zhao P-y, Wang L-l, Lin Y, Lv Y-j (2017) Experimental study of mechanics and seepage characteristics of sandstones after liquid-nitrogen stimulation. J Nat Gas Sci Eng 47:11–21

Zhou Z, Jin Y, Zeng Y, Zhang X, Zhou J, Zhuang L, Xin S (2020) Investigation on fracture creation in hot dry rock geothermal formations of China during hydraulic fracturing. Renew Energy 153:301–313

Zou C, Yang Z, He D, Wei Y, Li J, Jia A, Chen J, Zhao Q, Li Y, Li J, Yang S (2018a) Theory, technology and prospects of conventional and unconventional natural gas. Pet Explor Dev 45(4):604–618

Zou Y, Li N, Ma X, Zhang S, Li S (2018b) Experimental study on the growth behavior of supercritical CO_2 -induced fractures in a layered tight sandstone formation. J Nat Gas Sci Eng 49:145–156